Ab initio insights into support-induced sulfur resistance of Ni-based reforming catalysts: supplementary information

Amit Chaudhari [a], Pavel Stishenko [a], Akash Hiregange [a], Christopher R. Hawkins [b], Misbah Sarwar [b], Stephen Poulston [b] and Andrew J. Logsdail [*a]

[a] *Cardiff Catalysis Institute, School of Chemistry, Cardiff University, Main Building, Park Place, Cardiff, CF10 3AT, United Kingdom.*
[b] *Johnson Matthey Technology Centre, Blount's Court, Sonning Common, Reading, RG4 9NH, United Kingdom.*
[*] *E-mail: LogsdailA@cardiff.ac.uk*

S1 Electronic Structure Calculations

S1.1 DFT Benchmarking

S1.1.1 Basis Set

The calculations in this manuscript were performed with FHI-aims versions 210618 and later, which were verified to yield consistent total energies and forces. All DFT+U calculations were performed with a patch, corresponding to the GitLab commit "a1ab632a0890b9a1c9373bbb1d75aa0f3faf4950", which contains software fixes for the use of refined Hubbard projectors consisting of a linear combination of the atomic and hydrogenic auxiliary basis functions. The light basis set was chosen to balance computational cost with the accuracy of the predicted bulk Ni vacancy formation energy ($\Delta E_{\text{Ni Vac}}$) in a $3\times3\times3$ supercell, relative to an experimental reference (1.79 eV)[1], calculated using:

$$\Delta E_{\text{Ni Vac}} = E_{\text{Defective Ni Bulk}} + E_{\text{Isolated Ni Atom}} - E_{\text{Stoichiometric Ni Bulk}} \tag{1}$$

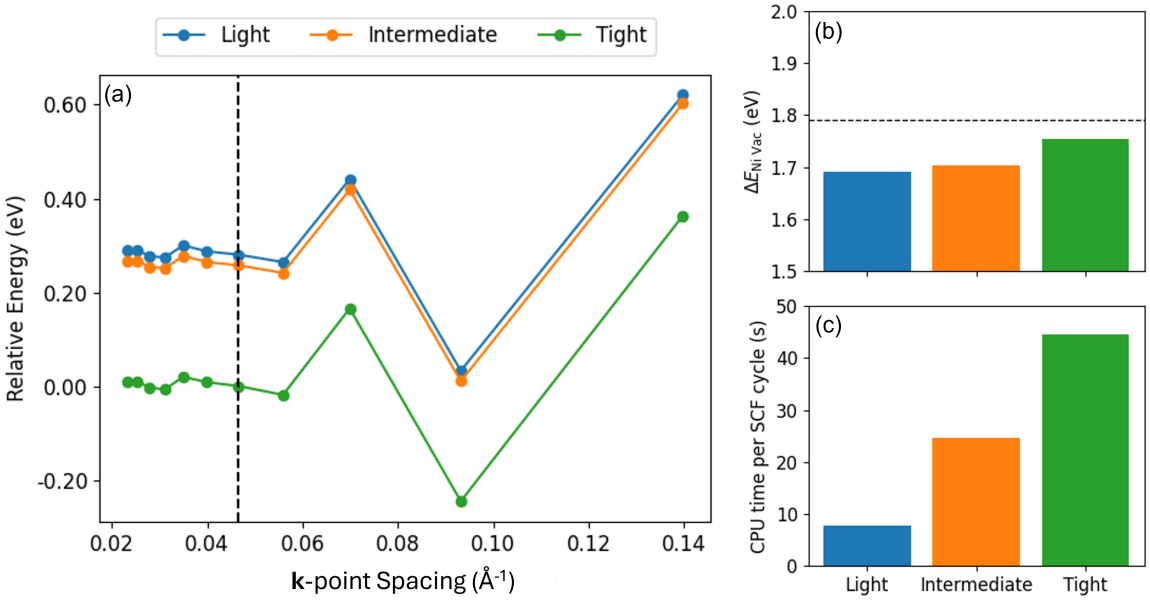

Figure S1: Comparing the effect of the basis set size on the (a) convergence of the relative total energy (*vs.* the converged value with the tight basis set) with respect to the **k**-point spacing, (b) the bulk Ni vacancy formation energy in a $3\times3\times3$ supercell and (c) the CPU time per SCF cycle for the bulk Ni vacancy geometry optimisation simulation (all calculated using the PBE functional). The black dashed line in (a) denotes the converged **k**-point spacing and in (b) denotes the experimental defect energy.[1]

S1.1.2 Exchange Correlation Density Functional

The accuracy of exchange correlation density functionals were assessed using the Euclidean norm of the percentage errors of the DFT-predicted $\Delta E_{\text{Ni Vac}}$, V_0 and cohesive energy (ΔE_{Coh}), relative to experimental references (1.79 eV,[1] 43.61421 Å^3 [2] and 4.48 eV/atom,[3] respectively):

$$E^{\text{Exc}} = \left\| \frac{100 \times (\Delta E_{\text{Ni Vac}} - \Delta E_{\text{Ni Vac}}^{\text{Exp}})}{\Delta E_{\text{Ni Vac}}^{\text{Exp}}}, \frac{100 \times (V_0 - V_0^{\text{Exp}})}{V_0^{\text{Exp}}}, \frac{100 \times (\Delta E_{\text{Coh}} - \Delta E_{\text{Coh}}^{\text{Exp}})}{\Delta E_{\text{Coh}}^{\text{Exp}}} \right\| \tag{2}$$

where the cohesive energy is defined as:

$$\Delta E_{\text{Coh}} = \frac{E_{\text{Ni atom}} - E_{\text{Ni bulk}}}{N} \tag{3}$$

where N is the number of atoms in the bulk. We chose the mBEEF meta-GGA exchange correlation density functional as it provides the best balance of accuracy in Table S1 among the tested meta-GGAs, and noting that less expensive GGAs are reported to provide insufficient accuracy for modelling sulfur adsorption complexes on transition metal surfaces with accuracy that matches experimental observations.[4]

Table S1: DFT-calculated Ni vacancy formation energy (ΔE_{vac}), unit cell equilibrium volume (V_0), cohesive energy (ΔE_{Coh}) and average error in Equation 2 E^{Exc} for a range of exchange correlation density functionals. Rows are ordered from top to bottom for increasing values of E^{Exc}. Experimental reference values are included for comparison.[1–3]

Functional	ΔE_{vac} (eV)	V_0 (Å^3)	ΔE_{Coh} (eV)	E^{Exc} (%)
PBE	1.69	43.17	5.66	26.92
mBEEF	1.74	41.15	5.90	32.39
rSCAN	1.96	41.22	6.29	41.93
PBEsol	2.09	41.22	6.27	43.67
SCAN	1.97	40.84	6.46	45.66
BLYP	0.90	45.32	4.81	50.25
LDA	2.26	39.87	6.68	56.36
M06-L	2.88	42.08	6.55	76.44
Exp	1.79	43.61	4.48	N/A

S1.1.3 Ni(111) Surface Model

The pristine Ni(111) surface was modelled using a six layer symmetric periodic slab, of which the bottom three layers were frozen to mimic the system bulk, which is in line with computational literature studying the adsorption of catalyst poisons on Ni(111).[5] Our periodic slab model yields a converged surface energy γ^{surf} of 1.73 Jm^{-2}, which is in reasonable agreement with experimental references (1.94 Jm^{-2}), as shown in Figure S2.[6] γ^{surf} is defined as:[7]

$$\gamma^{\text{surf}} = \gamma^{\text{cleave}} + \gamma^{\text{relax}} = \frac{E_{\text{Ni slab}}^{\text{Unrelaxed}} - N^{\text{Form}} \times E_{\text{Ni bulk}}}{2 \times A} + \frac{E_{\text{Ni slab}}^{\text{Relaxed}} - E_{\text{Ni slab}}^{\text{Unrelaxed}}}{A} \tag{4}$$

where $E_{\text{Ni slab}}^{\text{Relaxed}}$ ($E_{\text{Ni slab}}^{\text{Unrelaxed}}$) denotes the energy of the geometry optimised (initial) Ni slab, $E_{\text{Ni bulk}}$ denotes the energy of the geometry optimised Ni bulk, N^{Form} denotes the number of formula units in

the slab and A denotes the slab surface area.

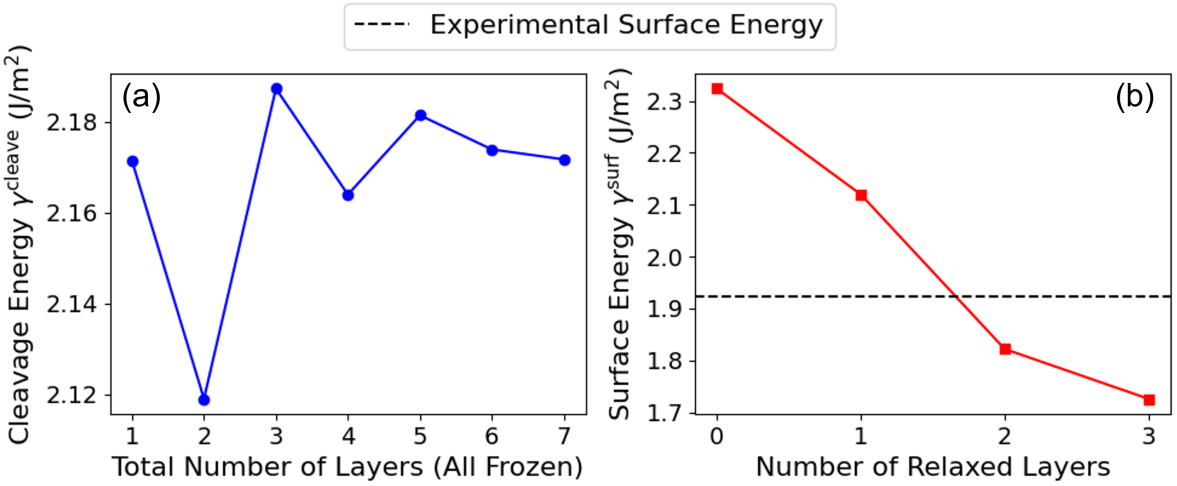

Figure S2: Convergence tests for the (a) cleavage energy and (b) surface energy of the Ni(111) periodic slab model used in this work, as defined in Equation 4.

S1.1.4 Adsorption Energies on Ni(111)

Table S2: Adsorption energies (ΔE_{Ads}, eV) for atomic S, atomic O, molecular SO (for S binding to surface and OS for O binding to the surface) and molecular SO_2 on a 1 × 1 Ni(111) surface, calculated using DFT with the mBEEF exchange correlation density functional. The active sites are (1) hollow HCP, (2) hollow FCC, (3) atop and (4) bridge, as illustrated in Section 3.1, Figure 2. Available literature comparisons are included with the corresponding exchange correlation density functional in brackets. Our results match the relative stabilities of adsorption complexes between active sites, but differences in absolute adsorption energies *vs*. the available literature are noted due to the use of GGA exchange correlation density functionals and different Ni(111) surface parameters, *e.g.*, number of layers and supercell dimensions.

Adsorbate	Active Site	ΔE_{Ads} (eV)	Literature
S	1	-7.09	-5.07 (PW91)[8], -4.57 (RPBE)[8], -5.56 (PBE)[9], -5.16 (PBE)[10]
S	2	-7.14	-5.12 (PW91)[8], -4.62 (RPBE)[8], -4.69 (RPBE)[11], -5.62 (PBE)[9], -5.21 (PBE)[10]
O	1	-6.25	-5.02 (PW91)[8], -4.42 (RPBE)[8], -5.76 (PBE)[9], -5.91 (PBE)[10]
O	2	-6.48	-5.13 (PW91)[8], -4.52 (RPBE)[8], -5.87 (PBE)[9], -6.02 (PBE)[10]
SO (OS)	1	-4.62 (-2.27)	N/A
SO (OS)	2	-4.64 (-2.54)	-2.08 (PW91)[12]
SO_2	3	-2.00	-1.03 (PBE)[10]
SO_2	4	-2.08	-1.08 (PBE)[10]

S1.2 DFT+U Parameterisation

To accurately parameterise DFT+U, one must account for both the magnitude and basis of the Hubbard correction, which are defined using the Hubbard U value and the Hubbard projector function (or Hubbard projector), respectively.[13,14] These parameters are used to correct the DFT-predicted total energy (E_{DFT}) with a corrective Hubbard term that treats localised states only (E_U^0) and a double counting correction (E_U^{dc}) that prevents the double counting of localised states in both E_{DFT} and E_U^0:

$$E_{\mathrm{DFT}+U}[\rho(\mathbf{r}), \mathbf{n}_{I,m}^{\sigma}] = E_{\mathrm{DFT}}[\rho(\mathbf{r})] + E_U^0[\mathbf{n}_{I,m}^{\sigma}] - E_U^{\mathrm{dc}}[\mathbf{n}_{I,m}^{\sigma}] \tag{5}$$

where $\rho(\mathbf{r})$ is the electron density and $\mathbf{n}_{I,m}^{\sigma}$ is the occupation matrix, whose diagonal elements correspond to orbital occupation numbers for all atoms (I), orbital magnetic quantum numbers (m) and spin channels (σ). According to the rotationally invariant, spherically averaged implementation proposed by Dudarev *et al.*,[15] the corrective Hubbard term is calculated using the trace (Tr) of the occupation matrix and its square:

$$E_U^0[\mathbf{n}_I^{\sigma}] = \sum_{(\sigma,I)} U^I \left[\mathrm{Tr}(\mathbf{n}_I^{\sigma}) - \mathrm{Tr}(\mathbf{n}_I^{\sigma}\mathbf{n}_I^{\sigma})\right] \tag{6}$$

The occupation matrix is calculated by projecting all DFT-predicted Kohn-Sham states onto the Hubbard projectors,[13] which were modified from the default atomic functions for both Ti 3d and Ce 4f orbitals to ensure self-consistent resolution of the DFT+U occupation matrices when modelling point defects, as discussed in previous work.[14] Modified atomic-like Hubbard projectors were constructed as a linear combination of the corresponding atomic and hydrogenic auxiliary basis functions in the light basis set, where the auxiliary basis function is subject to a Gram–Schmidt orthogonalisation with respect to the atomic function. The linear combinations were defined using the linear expansion coefficients c_1 and c_2, respectively, and were simultaneously optimised with Hubbard U values using a machine learning-based workflow that targets the bulk material covalency, as calculated using hybrid-DFT.[14] The Hubbard U values and projector coefficients c_1 and c_2 used in this work are listed in Table S3.

Table S3: Parameterised Hubbard U values (eV), projector coefficients c_1 and c_2 and supercell sizes used in this work.

Support Material	Corrected Orbital	Hubbard U (eV)	c_1	c_2	Supercell Size
γ-Al_2O_3	N/A	N/A	N/A	N/A	1×1×3
TiO_2	Ti 3d	2.575	0.752	-0.486	2×2×5
CeO_2	Ce 4f	2.653	0.561	-0.600	2×2×3

The DFT- and DFT+U-predicted band gap (E_{bg}), V_0 and formation energy (ΔE_{Form}) of each material are compared with experimental references in Table S4. Here, ΔE_{Form} is calculated using the energies of bulk Ti (in the hexagonal close packed, HCP, crystal structure), bulk Al and Ce (both in the cubic

crystal structure) and an isolated O_2 molecule:

$$\Delta E_{\text{Form}} = E_{\text{MO}_x} - E_{\text{M}} - x \times E_{\text{O}_2} \tag{7}$$

Table S4: DFT- and DFT+U-predicted geometric, electronic and energetic properties of bulk γ-Al_2O_3, rutile TiO_2 and CeO_2 versus experimental references. The Hubbard parameters for Ti 3d orbitals are U = 2.575 eV, c_1 = 0.752 and c_2 = -0.486, whilst those for Ce 4f orbitals are U = 2.653 eV, c_1 = 0.561 and c_2 = -0.600. No Hubbard correction is applied for γ-Al_2O_3 or Ni in this work.

Material	Method	E_{bg} (eV)	V_0 (Å^3)	ΔE_{Form} (eV/Atom)
γ-Al_2O_3	DFT	5.66	371.77	-3.22
γ-Al_2O_3	Experimental	7.20 [16]	371.12 [17]	-3.43 [18]
TiO_2	DFT+U	2.47	62.86	-3.00
TiO_2	Experimental	3.00 [19]	62.44 [20]	-3.26 [21]
CeO_2	DFT+U	2.38	159.95	-3.73
CeO_2	Experimental	3.20 [22]	158.43 [23]	-3.77 [24]

S2 Many-Body Tensor Representations

Two-body many-body tensor representations (MBTRs)[25] were evaluated using the *DScribe* Python library.[26,27] Pairwise interatomic distances between adsorbed S and O atoms were encoded as a smooth density distribution over a continuous grid, defined over the range of 0 to 10 Å, with a Gaussian broadening parameter set to 0.1. An exponential weighting function was applied with a decay scale of 0.5, as well as a threshold of 10^{-3}, which acts as a cutoff for discarding small Gaussian contributions and therefore emphasise closer atomic interactions. No normalisation was applied to preserve the raw spatial distributions. The smooth density distribution was discretised into five equally spaced bins, yielding five two-body MBTR descriptors (D_i), before being reduced to a one-dimensional descriptor using principal component analysis (PCA) with the *Scikit-learn* Python library.[28] The principal component output from PCA (PC^{MBTR}) is defined as:

$$\text{PC}^{\text{MBTR}} = (0.4852 \times D_2) + (0.5003 \times D_3) + (0.5070 \times D_4) + (0.5071 \times D_5) \tag{8}$$

where D_i denotes the discretised MBTR descriptors and $D_1 = 0$ as short-range S-O interactions are excluded from the GCMC sampling and therefore not present in the resulting adlayers. PC^{MBTR} therefore captures the most significant trends in the spatial disorder of co-adsorbed S and O.

S3 MACE Optimisation of GCMC Adlayers

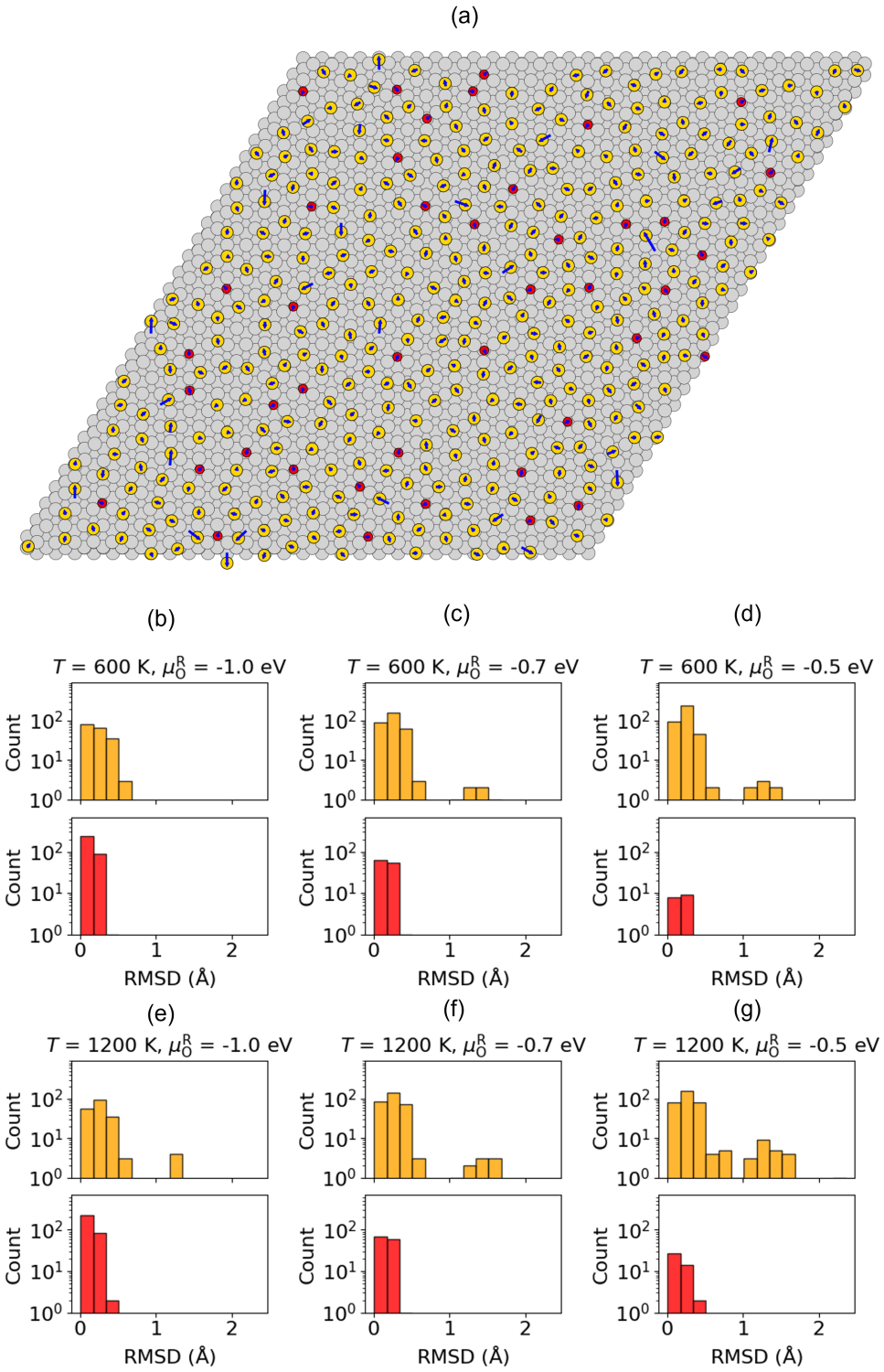

Figure S3: (a) The MACE-reoptimised structure for the GCMC-predicted adlayer for μ_S^R = -1 eV, μ_O^R = -0.5 eV and T = 1200 K, which corresponds to the largest RMSD in Section 3.2, Figure 4(d). The arrows indicate the direction and magnitude of atomic S and O displacements from the initial GCMC-predicted atomic positions. (b)-(e) Histograms of RMSD of S (yellow bars) and O (red bars) atoms between the GCMC-predicted and MACE-reoptimised adlayers for all six validated adlayers in Section 3.2, Figure 4(d).

S4 Scanning Electron Microscopy

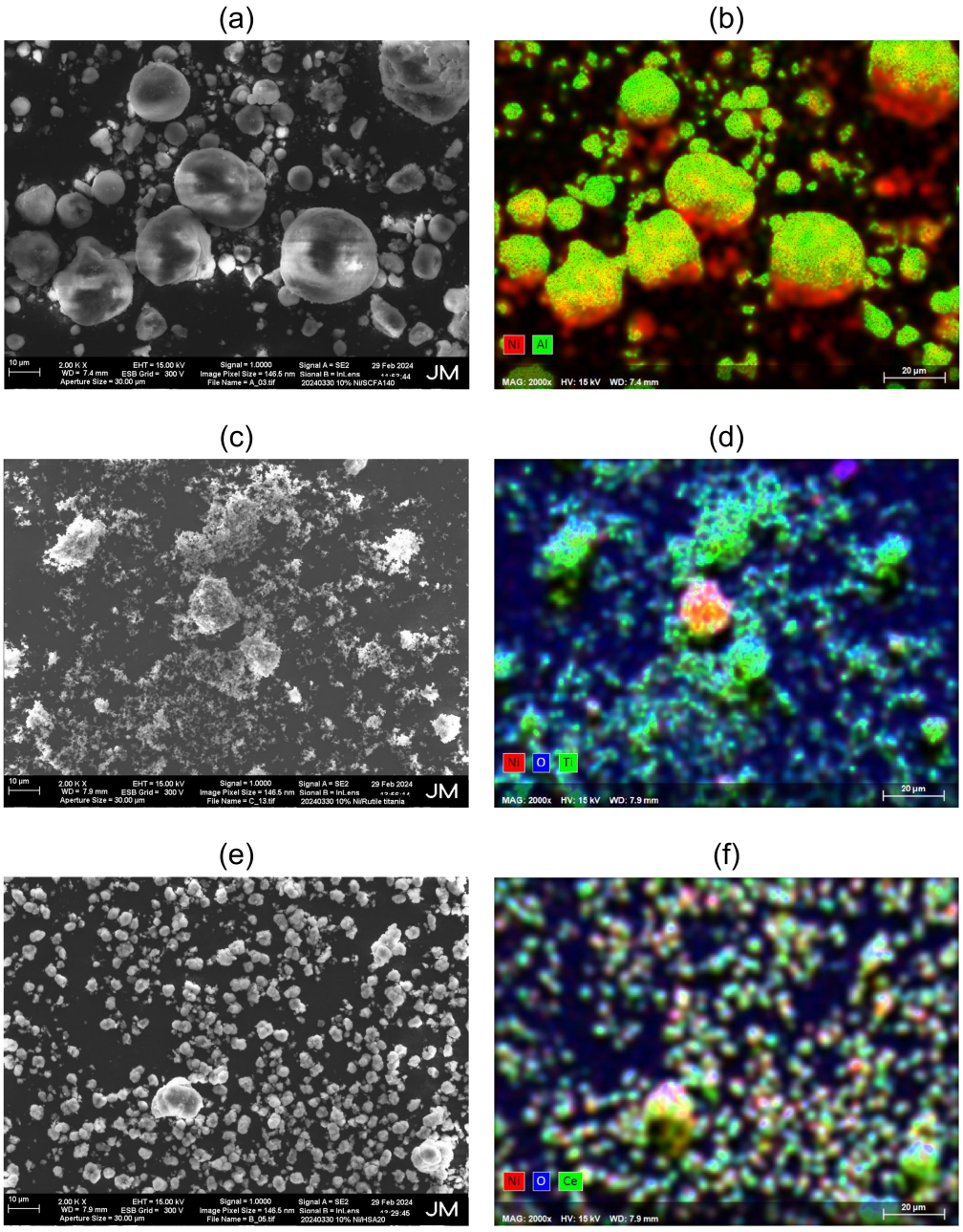

Figure S4: Scanning electron microscopy images of the microstructure of the prepared (a) Ni/γ-Al_2O_3, (c) Ni/TiO_2 and (e) Ni/CeO_2 catalysts. The corresponding elemental mapping of Ni (red), O (blue) and either (b) Al, (d) Ti or (f) Ce (green) shows the variation in the Ni dispersion amongst the prepared catalysts, which is significantly lower for Ni/TiO_2.

Notes and references

1 B. Medasani, M. Haranczyk, A. Canning and M. Asta, *Comput. Mater. Sci.*, 2015, **101**, 96–107.

2 M. Asadikiya, V. Drozd, S. Yang and Y. Zhong, *Mater. Today Commun.*, 2020, **23**, 100905.

3 P. Janthon, S. A. Luo, S. M. Kozlov, F. Viñes, J. Limtrakul, D. G. Truhlar and F. Illas, *J. Chem. Theory Comput.*, 2014, **10**, 3832–3839.

4 P. M. Spurgeon, D.-J. Liu, J. Oh, J. W. Evans and P. A. Thiel, *Sci. Rep.*, 2019, **9**, 19842.

5 S. S. Yadavalli, G. Jones and M. Stamatakis, *Phys. Chem. Chem. Phys.*, 2021, **23**, 15601–15612.

6 H. Meltzman, D. Chatain, D. Avizemer, T. M. Besmann and W. D. Kaplan, *Acta Mater.*, 2011, **59**, 3473–3483.

7 J. C. Boettger, *Phys. Rev. B*, 1994, **49**, 16798–16800.

8 Y. Bai, D. Kirvassilis, L. Xu and M. Mavrikakis, *Surf. Sci.*, 2019, **679**, 240–253.

9 V. Alexandrov, M. L. Sushko, D. K. Schreiber, S. M. Bruemmer and K. M. Rosso, *Corros. Sci.*, 2016, **113**, 26–30.

10 L. Liu, C. Zhang, W. Wang, G. Li and B. Zhu, *Molecules*, 2023, **28**, 6739.

11 C. R. Bernard Rodríguez and J. A. Santana, *J. Chem. Phys.*, 2018, **149**, 204701.

12 N. K. Das and W. A. Saidi, *J. Chem. Phys.*, 2017, **146**, 154701.

13 M. Kick, K. Reuter and H. Oberhofer, *J. Chem. Theory Comput.*, 2019, **15**, 1705–1718.

14 A. Chaudhari, K. Agrawal and A. J. Logsdail, *Digit. Discov.*, 2025, **4**, 3701–3727.

15 S. L. Dudarev, G. A. Botton, S. Y. Savrasov, C. J. Humphreys and A. P. Sutton, *Phys. Rev. B*, 1998, **57**, 1505–1509.

16 R. H. French, *J. Am. Ceram. Soc.*, 1990, **73**, 477–489.

17 S. Wilson, *J. Solid State Chem.*, 1979, **30**, 247–255.

18 S. Carstens, R. Meyer and D. Enke, *Materials*, 2020, **13**, 1787.

19 L. Kavan, M. Grätzel, S. E. Gilbert, C. Klemenz and H. J. Scheel, *J. Am. Chem. Soc.*, 1996, **118**, 6716–6723.

20 T. Arlt, M. Bermejo, M. A. Blanco, L. Gerward, J. Z. Jiang, J. Staun Olsen and J. M. Recio, *Phys. Rev. B*, 2000, **61**, 14414–14419.

21 M. Arrigoni and G. K. H. Madsen, *J. Chem. Phys.*, 2020, **152**, 044110.

22 S. Phoka, P. Laokul, E. Swatsitang, V. Promarak, S. Seraphin and S. Maensiri, *Mater. Chem. Phys.*, 2009, **115**, 423–428.

23 L. Gerward, J. Staun Olsen, L. Petit, G. Vaitheeswaran, V. Kanchana and A. Svane, *J. Alloys Compd.*, 2005, **400**, 56–61.

24 F. B. Baker, E. J. Huber, C. E. Holley and N. Krikorian, *J. Chem. Thermodyn.*, 1971, **3**, 77–83.

25 H. Huo and M. Rupp, *Mach. Learn.: Sci. Technol.*, 2022, **3**, 045017.

26 L. Himanen, M. O. J. Jäger, E. V. Morooka, F. Federici Canova, Y. S. Ranawat, D. Z. Gao, P. Rinke and A. S. Foster, *Comput. Phys. Commun.*, 2020, **247**, 106949.

27 J. Laakso, L. Himanen, H. Homm, E. V. Morooka, M. O. J. Jäger, M. Todorović and P. Rinke, *J. Chem. Phys.*, 2023, **158**, 234802.

28 F. Pedregosa, G. Varoquaux, A. Gramfort, V. Michel, B. Thirion, O. Grisel, M. Blondel, P. Prettenhofer, R. Weiss, V. Dubourg, J. Vanderplas, A. Passos, D. Cournapeau, M. Brucher, M. Perrot and E. Duchesnay, *J. Mach. Learn. Res.*, 2011, **12**, 2825–2830.